ELSEVIER

Polymer 41 (2000) 771–786

polymer

Biaxial hot drawing of poly(ethylene terephthalate): measurements and modelling of strain-stiffening

A.M. Adams[a], C.P. Buckley[a,*], D.P. Jones[b]

[a]*Department of Engineering Science, University of Oxford, Parks Road, Oxford OX1 3PJ, UK*
[b]*DuPont (UK) Ltd, PO Box 2002, Wilton, Middlesbrough TS90 8JF, UK*

Received 5 October 1998; accepted 17 November 1998

Abstract

A previous study of hot-drawing of amorphous films of poly(ethylene terephthalate) under biaxial stress (Polymer 1996;37:2403) was extended to compare constant width (CW) and equal biaxial (EB) strain states, with special emphasis on the pronounced strain-stiffening that begins at draw ratios of approximately 2. Some as-drawn specimens were also studied by density measurement and wide-angle X-ray scattering. Stress–strain data were obtained during drawing at a constant extension-rate of 1/s, across the temperature range between the glass transition and terminal regions. They were interpreted in terms of the multiaxial glass–rubber constitutive model proposed before, and the CW and EB stress–strain relations for the PET rubber-like entanglement network were extracted. The information was then used to quantify the entanglement slippage superposed on deformation of the network at higher temperatures. This revealed anomalous behaviour: entanglement slippage was found to arrest spontaneously at a critical level of orientation, associated with the first appearance of crystallinity in the drawn specimens. The constitutive model was extended to incorporate these features, with the arrest of entanglement slippage entering the model via a viscosity increasing asymptotically at a critical maximum principal network stretch. The model was then able to capture strain-stiffening behaviour through the temperature range.

Keywords: Poly(ethylene terephthalate); Biaxial drawing; Constitutive model

1. Introduction

Biaxial hot-drawing of amorphous poly(ethylene terephthalate) is an integral feature of some important industrial processes, for example thermoforming, bottle stretch-blow moulding and biaxial film drawing. The purpose is to optimise thermomechanical stability of the product by imparting biaxial in-plane molecular orientation. It is carried out on a time/temperature scale which extends from the vicinity of the glass transition upward through the rubber–elastic plateau region to the terminal (viscous flow) region, and is complicated by the occurrence of stress-induced crystallisation. With so many physical processes involved, to understand their separate roles and to make quantitative predictions of polymer constitutive behaviour during these orientation processes present major challenges.

The first challenge is to obtain reliable measurements of constitutive response during biaxial drawing of PET, as they require specialised test equipment capable of imposing large stretches (strains of order 3), under known biaxial stress conditions. These are difficult experiments and the literature is sparse.

The first systematic study of this type was reported by Chandran and Jabarin [1–3], who compared stress–strain relations measured during simultaneous and sequential biaxial drawing, and showed that stress-induced crystallisation and consequent changes in various physical properties, appear to be associated in some way with strain-stiffening in this polymer: a point to which we return in the present article. Buckley et al. [4] examined the effect of varying temperature and strain-rate on constant-width drawing, as compared to uniaxial drawing, and showed how a glass–rubber constitutive model (see below) could be fitted to the data at the lower end of the temperature range of practical interest (ca. 80°C) but not at higher temperatures. Mathews et al. [5] studied in detail the early parts of the stress–strain relations (prior to strain-stiffening) for uniaxial, constant-width and equal biaxial (EB) drawing, and showed how they could be fitted consistently at a particular temperature (85°C) by a theory of rubber elasticity, provided the number density of network junction points was allowed to vary with octahedral shear-rate. Zaroulis and Boyce [6] reported

* Corresponding author. Tel.: +44-1865-273156; fax: +44-1865-273906.
E-mail address: paul.buckley@eng.ox.ac.uk (C.P. Buckley)

0032-3861/00/$ - see front matter
PII: S0032-3861(98)00834-9

recently on uniaxial and constant-width compression tests on amorphous PET, including some tests in the glass transition region. By means of DSC on the latter specimens they provided further evidence for the link between strain-stiffening and stress-induced crystallisation.

Given the major industrial importance of orientation processing of PET, there is an urgent need to understand better the relationships between molecular orientation, crystallisation and strain-stiffening in the hot drawing of this polymer. In particular, the practical need is for a physically based constitutive model that will encompass the full range of behaviour exhibited by PET during industrial drawing processes. In constructing such a model, our starting point is the observation by Pinnock and Ward [7], confirmed in several publications since [4,5,8–11], that in certain respects uncrosslinked amorphous PET in this time/temperature regime shows the features of a network polymer above the glass transition, and under certain circumstances its constitutive response is amenable to analysis in terms of the theory of rubber-like entropic elasticity. This is, however, an incomplete picture. Hot-drawing processes of practical interest occur close to the glass transition, and the contribution of stress arising from perturbation of inter-atom potentials is not always fully relaxed on the experimental time-scale. For a more comprehensive analysis of deformation in amorphous PET, and in other amorphous polymers in the region of and just above the glass transition, it is necessary to include this addition to the drawing stress [7,12]. This recognition was the basis of the Haward–Thackray [13] one-dimensional mathematical model that accounts qualitatively for the observed uniaxial drawing behaviour of amorphous polymers. It combines a flow stress of Eyring-type with a rubber–elastic stress of the classical inverse-Langevin type.

More recently there has been a revival of interest in this approach, as the basis of three-dimensional constitutive models of polymer behaviour, for use in computer-based analyses of products and processes. Such constitutive models represent the material by a system of nonlinear simultaneous differential equations that are solved numerically with a time-marching scheme. Three-dimensional constitutive models have been proposed for describing aspects of glassy polymers [14–16] and crosslinked rubbery polymers [17]. For amorphous polymers in the vicinity of the glass transition (above or below), Buckley and Jones suggested a model of "glass–rubber" type, that captures a wide range of observed features of amorphous polymers on either side of the transition [18]. This model was employed in the present work.

It has been applied already to hot-drawing of PET under biaxial stress by Buckley et al. [4], and found to give a good description of amorphous PET for deformation rates about 1/s and temperatures close to the glass transition (ca. 70°C). However for these deformation rates, when temperatures exceeded ca. 80°C, a significant discrepancy appeared in the pattern of strain-stiffening seen at large strains. Here, the entropic "rubber-like" contribution to stress was found to be no longer a unique function of total stretch, as expected of a true molecular network, and as assumed by the model. Specifically, measured drawing stresses in the strain-stiffening region revealed a deficit when compared to predictions of the glass–rubber constitutive model [4]. The deficit increased during drawing and became more pronounced with increasing temperature. Buckley et al. attributed this result to the onset of viscous flow because of "entanglement slippage" [4]. By this is meant axial diffusion of whole molecules, whereby constraint from entanglements is relaxed – the process of reptation. The proportion of the stretch associated with such viscous flow would be expected to increase with temperature as viscosity falls, leading to loss of correlation between the entropic stress and the total stretch. This observation is of vital importance for the modelling of PET processes, as the range of drawing rates and temperatures of practical significance embraces those where the stress deficit occurs. Clearly, entanglement slippage must be included in the model, and its effects must be allowed for when fitting the model to experimental data.

A second feature is also missing from the constitutive model as applied to PET: the stress-induced crystallization referred to above that intervenes at draw ratios of 2–3. Indeed, this crystallization is of technological importance as it allows molecular orientation to be "locked-in", providing enhanced in-plane strength, stiffness and dimensional stability. As yet, however, it is unclear how the constitutive response is modified by such structural change. The issue is of considerable importance. It must be resolved before there is any chance of extending constitutive modelling to encompass thermomechanical response subsequent to drawing, for example during further deformation in industrial drawing processes of the sequential biaxial type (stretch blow-moulding of bottles and sequential biaxial drawing of films).

The purpose of the present article is to quantify the roles of these additional features in the biaxial hot-drawing of amorphous PET, especially in the strain-stiffening region, and to extend the constitutive model to incorporate them. Specifically, we report further measurements of the hot drawing of PET film under biaxial stress, and use the data to isolate more carefully than hitherto the stress–strain relation of the entanglement network before slippage commences, and to quantify the contribution of entanglement slippage when it commences. This reveals an interesting result: the viscous flow because of entanglement slippage in PET shows anomalous behaviour, whose explanation is to be found in structural change. Finally we suggest modifications to the constitutive model whereby all these effects can be combined, and the biaxial stress–strain response modelled over the full time/temperature range of interest. The present work forms part of a wider study aimed at physically based modelling of biaxial orientation processes for polymers, of which an overview is given elsewhere [19].

2. Experiments

2.1. Material

The polymer used was ICI PET homopolymer with number average molecular weight $M_n = 19\,000$, and diethylene glycol content of only 2.7 mol%. Isotropic amorphous film was prepared by melt extrusion through a slit die onto a chilled roller held at 10°C, and then wound up to produce a film with nominal thickness 250 μm. The measured density was 1338 kg/m^3 and wide angle X-ray scattering (WAXS) showed no evidence for diffraction, indicating absence of crystallinity. The in-plane birefringence was found to be only 1.4×10^{-4} confirming that in-plane molecular orientation in the as-extruded film was negligible.

2.2. Experimental details

The biaxial drawing experiments were carried out with the Flexible Biaxial Film Tester (FBFT) used previously [4], with modifications described by Adams [20]. The FBFT was designed specifically for the biaxial testing of polymeric films under conditions comparable to those encountered in the manufacture of high performance films. In particular it provided for flexible experiment design, as the time-sequences of displacement on both axes of straining and of temperature are all under software control, and the machine was able to achieve the high rates of strain and temperature change seen under process conditions.

The FBFT had a horizontal biaxial stretching frame driven by two, crossed, reverse-thread leadscrews. In the present work, the specimen temperature was controlled by impingement on its top surface by a variable-temperature air-jet from a rotary mixing valve of the type described by Buckley and Sikorski [21], the air-jet being contained by a silicone rubber jacket surrounding the specimen and expanding with it during drawing. The bottom surface of the specimen was effectively thermally insulated, by air trapped by a rubber sheet that expanded with the specimen during drawing. In this manner, heat transfer coefficients of 40 and 2.5 W/m^2 K were achieved on upper and lower faces of the specimen respectively, ensuring through-thickness temperature variations within the specimen were less than 0.5 K. Non-uniformity in the air-jet temperature at the specimen was 1 K prior to straining. Specimen temperature was calibrated in terms of the air-jet temperature using a dummy specimen with embedded thermocouple. During an experiment (typically of duration 3 s), measurements of load on one of the centre grips on each axis, and the air-jet temperature, were continuously logged by a Biodata Microlink interface and fed to the control computer, for calculation of nominal stress on each axis and the specimen temperature. True stresses were calculated on the assumption that drawing took place at constant volume.

The following experimental procedure was adopted. First the 70 mm square film specimen was marked with an ink grid using a computer plotter. It was then mounted in the grips of the FBFT and soaked in blown air at the test temperature for 5 min, before initiation of drawing. In the present study, all drawing tests consisted of proportional straining: motion on the two axes started and stopped simultaneously, and the speeds were constant and in a ratio θ. Most tests were either at CW ($\theta = 0$), or simultaneous EB ($\theta = 1$), and a few additional tests were non-equal biaxial (NEB) with $\theta = 2$. Thus the nominal strain-rate on axis 1 was kept fixed at 1/s, while that on axis 2 was 0, 1 or 2/s: the final nominal in-plane strains varying between 0 and 3.4. On completion of straining, after a delay of no more than 0.5 s the heat valve was closed rapidly, quenching the specimen to room temperature before its removal from the test rig. There was no detectable strain recovery at room temperature. The grid was therefore used to measure the final deformation of the specimen, and to calibrate clamp separation in terms of strain, assuming a constant ratio between them throughout the test. At the rates of straining employed in the present work, it cannot be assumed that the tests were completely isothermal. The time constant for convective heat transfer varied from ca. 16 s initially, down to ca. 1 s at the highest strains in EB tests, while tests were of 3 s or less in duration. Calculations showed, however, that the effects on stress–strain curves of adiabatic heating during the experiments were small, and they were neglected in interpretation of the data.

To assist with interpretation of results, density measurements were made on representative samples cut from drawn film specimens, using a calcium nitrate and water density gradient column. Specimens were drawn to various strains at biaxiality ratios θ of 0, 1, 2 at $T = 86$°C, and $T = 97$°C. After straining, specimens were quenched immediately to below the glass transition temperature. The rate of quenching depended on the final area and shape of the sample, because of the variable geometry of the jacket. At low strains the air temperature was decreasing by 16°C/s, whereas at high strains this cooling rate was reduced to approximately 7°C/s. Strain was calculated from the local deformation of the square grid marked onto the specimen before drawing.

In addition, some WAXS patterns were obtained from specimens CW drawn at 97°C to various strains and quenched, with the X-ray beam normal to the draw direction and either perpendicular or parallel to the film plane.

2.3. Results

The effects of varying temperature on the biaxial drawing of PET were studied with a series of simultaneous EB drawing tests spanning the temperature range 75°C–120°C, at an extension rate of 1/s on both axes, as described above. For comparison, a parallel set of experiments was carried out under CW conditions, with an extension rate of 1/s on axis

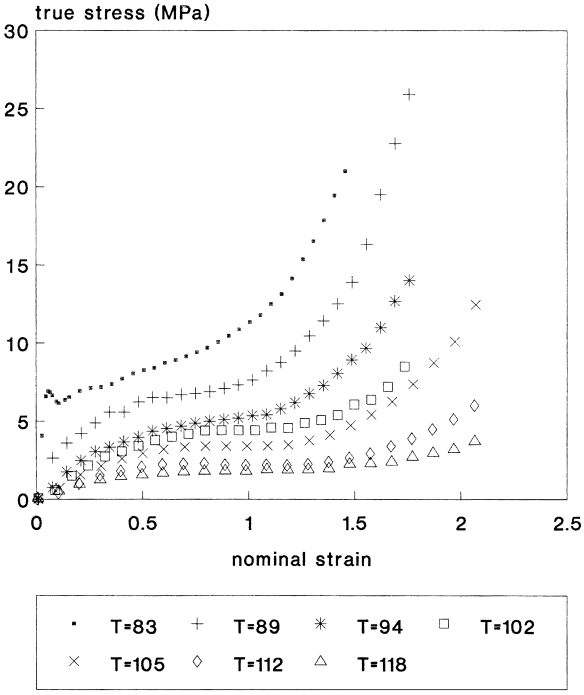

Fig. 1. Stress–strain curves measured during EB drawing of amorphous PET at a constant extension rate of 1/s, at the temperatures (°C) shown.

1. Representative data from these tests are shown in Figs. 1 and 2, where the pattern of evolution of the stress–strain data with temperature can be seen to mirror results obtained in the earlier study of CW and uniaxial drawing of PET [4]. In all cases, with increase in temperature the yield stress fell

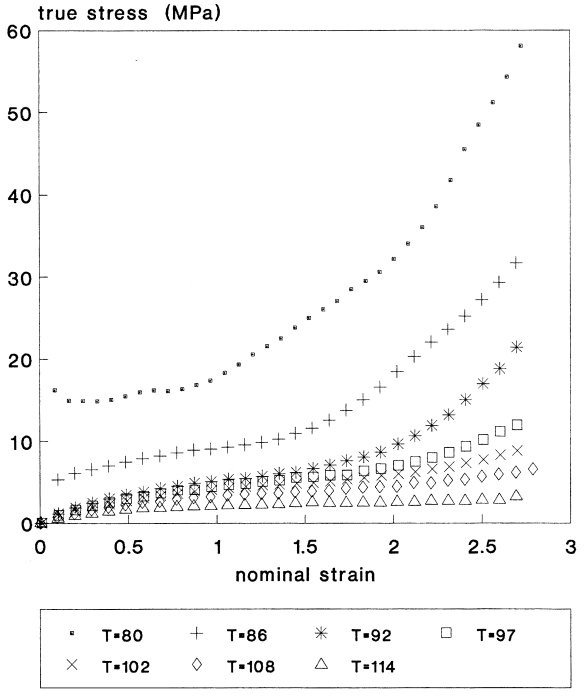

Fig. 2. As for Fig. 1, except for CW drawing.

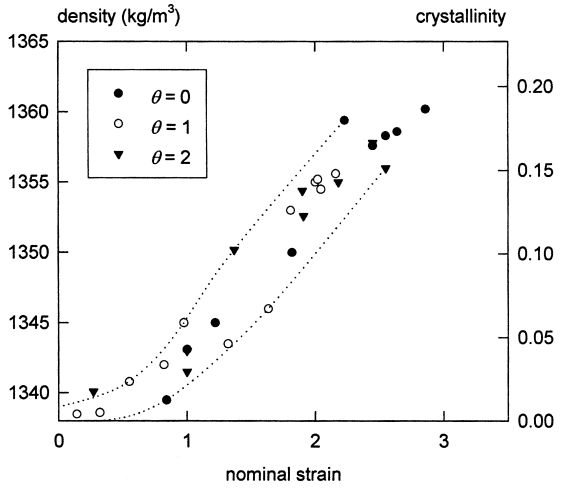

Fig. 3. Density measurements (left-hand scale) and apparent volume fraction degree of crystallinity (right-hand scale) for specimens of PET biaxially drawn at 86°C to various values of maximum principal strain, in strain states specified by biaxiality ratios θ shown.

and strain-stiffening was deferred to a later strain. Careful comparison of Figs. 1 and 2 also reveals a trend characteristic of polymers in the rubbery state: increasing the strain ratio θ from 0 to 1 (CW to EB) caused the onset of strain-stiffening at any given temperature to occur sooner. All these features were reproduced faithfully by the constitutive model, as shown later.

We have already reported an analysis of yield stresses measured in these tests, and with other strain ratios [22]. The variations of yield stresses on each axis with θ were found to agree closely with the glass–rubber constitutive model proposed before. This article focuses on the strain-stiffening part of the response.

Density measurements from specimens drawn to different extents at 86°C in experiments with the three values of strain ratio θ, are plotted together in Fig. 3, as a function of the maximum principal nominal strain. As can be seen, the data for different values of θ appear to be confined to a broad band, defined by the dotted lines drawn. A corresponding plot for a draw temperature of 97°C is given in Fig. 4, where the same trend is apparent but the rise in density is deferred to higher strain compared to Fig. 3. These graphs include as a right-hand scale the apparent volume fraction degree of crystallinity

$$\chi = \frac{\{\rho - \rho_a\}}{\{\rho_c - \rho_a\}} \tag{1}$$

calculated assuming values for the densities: fully amorphous isotropic PET $\rho_a = 1338$ kg/m^3 and the PET crystal unit cell $\rho_c = 1457$ kg/m^3. In view of the well-known tendency for ρ_a to rise with increasing orientation [23], however, the right-hand scale is intended for guidance only: whether the observed density increase can be attributed to crystallinity alone requires confirmation from other measurements. The distinctive sigmoidal increase of density

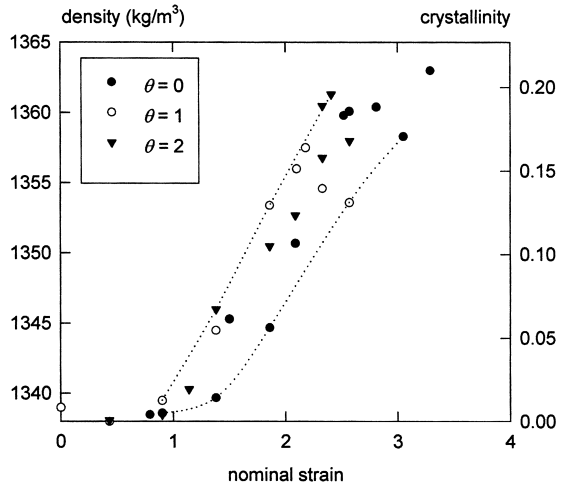

Fig. 4. As for Fig. 3, except for a draw temperature of 97°C.

of hot-drawn PET with increasing stretch has been reported before by several authors, and in particular was studied in detail by Salem and co-workers for uniaxial and constant-width drawing [24–26], and for biaxial drawing by Chandran and Jabarin [3].

Confirmation of structural change induced by drawing was provided by the WAXS patterns. They showed qualitative differences that are summarised in Table 1. Again these indicate trends noted by previous authors. The initial effect of drawing was to cause molecular orientation of the amorphous polymer parallel to the draw direction, but beyond a stretch of ca. 2 there were observable diffraction spots indicating long range order and hence crystallinity. The relative intensities of the diffraction spots revealed the well-known tendency of the phenyl rings (associated with the (1 0 0) crystal plane) to align in the film plane during drawing of PET under biaxial stress.

3. Interpretation of data in terms of constitutive model

3.1. Outline of the model including entanglement slippage

To avoid complexity that is superfluous to the present discussion, we consider here only irrotational displacements of the PET film, and hence the kinematics are fully described by a stretch tensor Λ whose eigenvalues are the principal stretches λ_i ($i = 1,3$). The constitutive model employed is based on that described by Buckley and Jones [18], and applied previously to PET [4,27]. The structure of the model is built on three key assumptions concerning the interaction of the various physical processes known to be active in the deformation of uncrosslinked amorphous polymers near their glass transitions.

Firstly, it is assumed that there are two independent sources for the change of free energy during deformation (we neglect here any possibility of a change of phase, but return to this question later). Consequently there are two contributions to the stress at any instant. They are a "bond-stretching" (b) contribution due to perturbation of inter-atom potentials, and a "conformational" (c) contribution due to perturbation of conformational statistics and hence of entropy. These two contributions to stress are assumed to have separate dependences on Λ and its history. Their superposition to give the total Cauchy stress can be expressed in terms of principal values

$$\sigma_i = \sigma_i^{\mathrm{b}} + \sigma_i^{\mathrm{c}} \qquad (i = 1\ldots3). \tag{2}$$

At the scale of individual molecular segments, it is known that the total stretch is divisible into a contribution due to elastic distortion (e) of inter- and intra-molecular primary and secondary bonds, and another due to viscoplastic flow (v) of segments past each other. The *second* key assumption of the model is that, following Lee [28], the elastic and viscous stretches combine multiplicatively:

$$\lambda_i = \lambda_i^{\mathrm{e}}\lambda_i^{\mathrm{v}} \qquad (i = 1\ldots3). \tag{3}$$

Conformational stress is determined by deformation on a larger scale: that of the entanglement network. However, when Buckley et al. [4] examined strain-stiffening during hot-drawing of PET, attributed to the conformational stress, they found that elastic stretch of a network of fixed properties could not account for the observed temperature-dependence. This is no surprise, as the PET is an uncrosslinked amorphous polymer approaching its terminal relaxation region, where entanglement slippage (by reptation) is expected to make a time/temperature-dependent addition to the total stretch. Hence, the total stretch can also be expressed in terms of the stretch of an elastic entanglement network (n), and flow because of slippage (s) of the

Table 1
Summary of features of Debye rings in WAXS patterns, observed following CW drawing to a stretch (draw ratio) λ at 97°C, followed by quenching to room temperature before release. Inequality signs indicate relative intensities of diffraction spots. The direction of the beam was normal to the draw direction, which lay on the meridian in the WAXS patterns. The onset of crystallinity in the drawn specimens occurs at $\lambda \approx 2$

	Beam perpendicular to film	Beam parallel to film
$\lambda = 1.38$	Diffuse scatter	Diffuse scatter
$\lambda = 1.74$	Diffuse scatter peaked on equator	Diffuse scatter peaked on equator
$\lambda = 2.33$	Diffraction spots peaked on equator (0 1 0) > ($\bar{1}$ 1 0) > (1 0 0)	Diffraction spots peaked on equator (1 0 0) > $\bar{1}$ 1 0) > (0 1 0)
$\lambda = 3.05$	Diffraction spots sharply peaked on equator (0 1 0) > ($\bar{1}$ 1 0) > (1 0 0)	Diffraction spots sharply peaked on equator (1 0 0) > ($\bar{1}$ 1 0) > (0 1 0)

entanglements, where the conformational free energy is determined by the elastic (network) stretch only. The *third* key assumption of the model is again that these combine multiplicatively:

$$\lambda_i = \lambda_i^{\mathrm{n}} \lambda_i^{\mathrm{s}}. \tag{4}$$

To complete the constitutive model, Eqs. (2)–(4) must be supplemented by expressions for the evolution of stresses σ_i^{b} and σ_i^{c} in terms of the stretches. Applying the model proposed previously [18], a set of equations can be established governing the evolution of the bond-stretching stresses. The hydrostatic part of this response is taken to be linear elastic with bulk modulus K^{b}. Defining the mean stress and volume ratio thus

$$\sigma_m^{\mathrm{b}} \equiv \frac{1}{3}\sum_{i=1}^{3} \sigma_i^{\mathrm{b}}, \qquad J \equiv \det \Lambda \tag{5}$$

the strain-induced hydrostatic stress was then given by

$$\sigma_m^{\mathrm{b}} = K^{\mathrm{b}} \ln J + \sigma_{m0}^{\mathrm{b}}, \tag{6}$$

where σ_{m0}^{b} is the initial, built-in, bond-stretching stress resisting collapse of the entropic network. The deviatoric stresses s_i^{b} exhibit viscoelasticity in terms of the deviatoric true strains:

$$\frac{\mathrm{d}s_i^{\mathrm{b}}}{\mathrm{d}t} + \frac{s_i^{\mathrm{b}}}{\tau} = 2G^{\mathrm{b}} \frac{\mathrm{d}e_i}{\mathrm{d}t}, \tag{7}$$

where

$$s_i^{\mathrm{b}} \equiv \sigma_i^{\mathrm{b}} - \sigma_m^{\mathrm{b}}, \qquad e_i \equiv \ln \lambda_i - \ln J^{1/3} \tag{8}$$

and the relaxation time τ is defined in terms of a generalised (stress-dependent) viscosity μ and the bond-stretching contribution to the shear modulus G^{b}:

$$\tau = \frac{\mu}{2G^{\mathrm{b}}}. \tag{9}$$

Buckley and Jones assumed that the viscous flow could be described as a three-dimensional thermally activated process of the Eyring type [29], and on that basis derived an expression for the viscosity μ in terms of temperature and the stress invariants.

Entropic elasticity of the entanglement network is expected to be highly nonlinear: this is the origin of strain-stiffening in amorphous polymers above the glass transition. It is convenient therefore to calculate the conformational stress directly by differentiation of the conformational free energy density A^{c}, thus:[1]

$$\sigma_i^{\mathrm{c}} = \frac{\lambda_i^{\mathrm{n}}}{J} \frac{\partial A^{\mathrm{c}}}{\partial \lambda_i^{\mathrm{n}}} \tag{10}$$

Edwards and Vilgis [30] derived an expression for A^{c} for the case of a network of freely orienting chains of finite length, where at least some of the junction points are of a physical nature with some freedom of movement (i.e. entanglements). As this is believed to describe the case of uncrosslinked PET, the Edwards–Vilgis expression was employed, in the limit where there are no chemical crosslinks:

$$A^{\mathrm{c}} = \frac{N_{\mathrm{s}} k_{\mathrm{B}} T}{2}\left(\frac{(1+\eta)(1-\alpha^2)}{(1-\alpha^2 \sum \lambda_i^{n2})} \sum \frac{\lambda_i^{n2}}{1+\eta\lambda_i^{n2}} + \sum \ln(1+\eta\lambda_i^{n2}) + \ln(1-\alpha^2 \sum \lambda_i^{n2}) \right), \tag{11}$$

where all the summations are over $i = 1\ldots3$, N_{s} is the density of "slip-links" representing entanglements, η is a parameter specifying the looseness of the entanglements ($\eta = 0$ for a crosslink), and α is a measure of the inextensibility of the entanglement network (α is related to the number n of freely orienting (Kuhn) segments per network chain: $\alpha = \sqrt{n^{-1}}$). Completion of the model requires a representation of the relaxation of conformational stress by entanglement slip: this issue is discussed later.

3.2. Experimental isolation of the rubber-like stress–strain relation

At temperatures close to the glass transition T_{g}, temperature-dependence enters the above equations predominantly through the viscosity μ, describing flow of segments relative to their neighbours. This falls rapidly with increasing temperature above T_{g}. Consequently Eq. (7) shows that, for a given constant strain-rate, the deviatoric bond-stretching components s_i^{b} are expected to become vanishingly small compared with the other contributions to stress, as temperature increases. If this occurs at temperatures below those where entanglement slippage intervenes, a polymer described by the above model exhibits a "rubber-like plateau", with entanglements acting as physical crosslinks. Here the word "plateau" refers to a time/temperature window where stress appears independent of time and temperature, for a given history of strain (we ignore here the slight temperature-dependence of A^{c} originating from its entropic nature). Such plateaux are a well-known feature of modulus-temperature plots for uncrosslinked amorphous polymers, provided the molecular weight exceeds the entanglement spacing [31]. Buckley et al. observed a similar plateau as an inflection in an isometric plot of stress versus temperature, measured during constant-width drawing experiments on PET [4], and used it to deduce the parameters of the conformational free energy function A^{c}, assuming that it was unaffected by the onset of entanglement slippage.

In the present work we have re-visited this question, to determine with more rigour than before the rubber-like response of PET, taking greater care to avoid the effects of entanglement slippage. Again we constructed isometric stress-temperature plots from stress–strain data obtained over a range of temperatures, such as shown in Figs. 1

[1] One of the superscripts n was inadvertently omitted from this equation in a previous outline of the model [19].

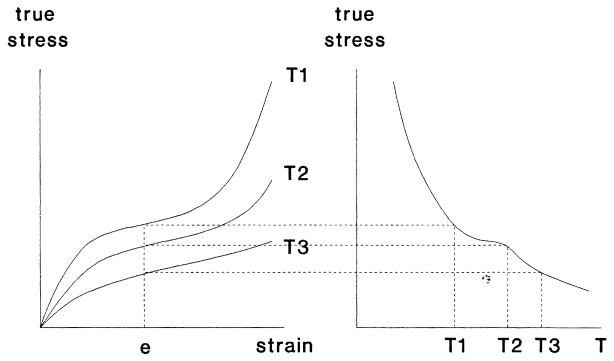

Fig. 5. Schematic diagram showing how isometric stress-temperature plots were calculated: (a) stress–strain curves for constant nominal strain-rate and various temperatures, and (b) isometric stress-temperature plot for a nominal strain *e*.

and 2. The principle of the procedure is outlined in Fig. 5. It was repeated for a range of strains *e*, for data from CW and EB drawing experiments, and Figs. 6 and 7 show example isometric plots from CW and EB drawing respectively. They clearly confirm the previous evidence for a distinct rubber − like plateau in PET, located at 95°C–100°C. However, they also confirm that the plateau is narrow: only ca. 5 K in width.

To summarise, the characteristic shape of the isometric plots can be explained thus. The initial decrease in stress is because of the decrease in the bond-stretch stress contribution with increasing temperature. A point is reached where this has decayed to zero, and therefore only the conformational contribution to the deviatoric stress remains, forming the plateau. At this strain and temperature, the rubber-like network is still intact. No entanglement slippage has occurred, and therefore the plateau stress is the entropy-elastic stress arising from hyper-elastic deformation of the network to a strain *e*, and a bond-stretching stress because of the small (but finite) volume change. In other words, the

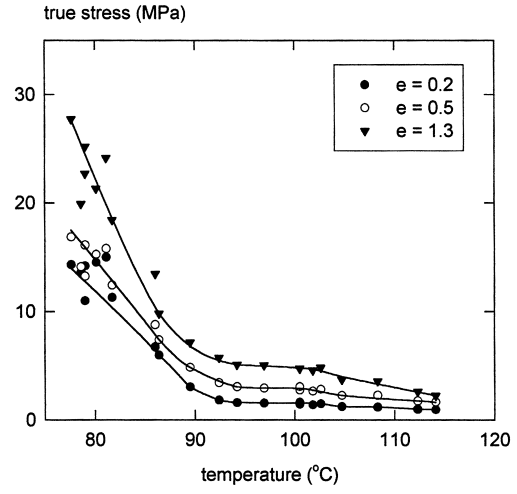

Fig. 6. Composite isometric plots for CW drawing to values of nominal strain shown.

polymer in this narrow region is behaving as a rubber, with entanglements acting as physical network junctions. As the temperature increases further, entanglement slippage becomes significant, and the stretch now has two components, one from stretch of the network and one resulting from entanglement slippage (reptation). As a result the elastic stretch of the network is reduced for a given value of *e*, resulting in a decrease in stress.

By taking the stresses at the plateaux for various *e* as the closest approximation to the rubber-like response of PET, apparent rubber-like stress–strain curves can be constructed, as illustrated for CW and EB drawing in Fig. 8. The difference in stiffness between the cases of CW and EB drawing is clearly in evidence. In fact the ratio of stresses EB : CW can be seen to be close to 1.5, as predicted by small strain isotropic linear elasticity. Unfortunately, the rubber-like stress–strain response of PET cannot be determined in this way over a wider range of strain, as it must be expected that with increasing strain (and hence time) there is progressive encroachment by entanglement slippage, making *e* increasingly unreliable as a measure of the elastic network strain at the plateau. For this reason, in isometric plots generated at higher strains the plateau disappears, as demonstrated in Fig. 9, obtained for CW drawing at a strain of 2.3. What are needed in determining the rubber-like response of PET are means (i) of identifying the onset of this perturbing influence, and (ii) of avoiding it.

The following strategy was found helpful. To minimise the effects of entanglement slippage on the results, experimental stress–strain data-sets obtained at the lower extreme of the temperature range (i.e. at ca. 80°C) was employed, as was carried out by Buckley et al. [4]. From these data were subtracted the apparent rubber-like stress values plotted in Fig. 8, to obtain the *apparent* strain-dependence of the bond-stretching stress. Results for three CW experiments are shown plotted versus true strain in Fig. 10, where an interesting anomaly is apparent. Beyond a critical strain close to 0.5, the apparent bond-stretching stress begins to rise rapidly. According to the Eyring model of flow, however, with parameters derived previously [4], the bond-stretching stress should fall linearly with increasing true strain with gradient shown by the dashed line in Fig. 10, because of the fall in rate of true strain in the present experiments which were conducted with constant rate of extension. At low strains there is good agreement with this prediction to within experimental scatter.

The conclusion is clear. Beyond a true strain of 0.5, the conformational stress as deduced from the plateau has been under-estimated (because of the onset of entanglement slippage) leading to the artefact of an apparently steeply rising bond-stretching stress in Fig. 10. The corollary also applies. For true strains below 0.5, the plateau does provide a good measure of the rubber-like stress–strain relation for PET.

On the basis of this evidence, the method described earlier [4] for finding the rubber-like stress–strain response

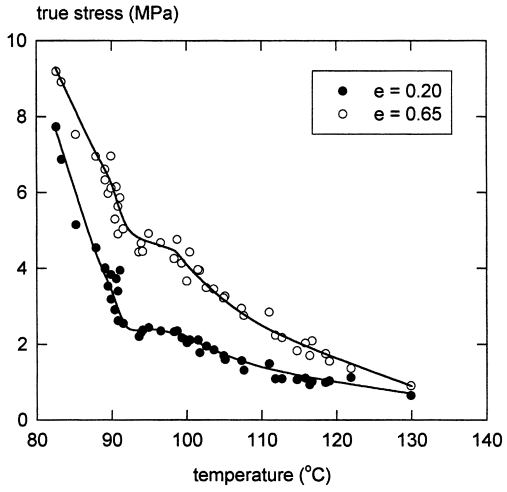

Fig. 7. As for Fig. 6, except for EB drawing.

of PET was applied again to the data obtained in the present study, but this time based on a plateau stress corresponding to a nominal strain of only 0.2. In brief the steps were as follows (details were given before [4]). (1) The plateau stress was used to deduce the rubber-like stress for a temperature of 80°C and nominal strain 0.2. (2) By subtraction from a measured stress–strain curve obtained at this temperature, the bond-stretch stress was found for this strain. (3) The bond-stretch stress for other strains was deduced from the Eyring model of flow, already known to fit the measured flow stress in PET [4,27]. (4) This was subtracted from the measured stress–strain curve to obtain the rubber-like curve for PET at 80°C.

The procedure was applied to the results from three CW drawing experiments, carried out at $T = 80 \pm 1$°C. A mean rubber-like stress–strain curve was then obtained, by averaging the stress value from the three curves over the whole strain range. This mean curve is shown in Fig. 11, together with the original data sets.

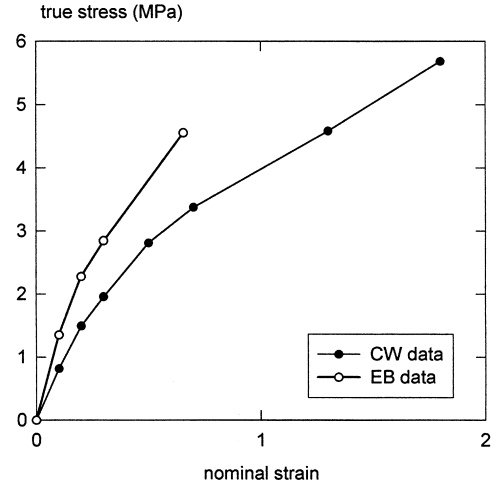

Fig. 8. Apparent curve of true stress versus nominal strain for the rubber-like elasticity of PET, as deduced from the plateaux observed in isometric stress-temperature plots (Figs. 6 and 7).

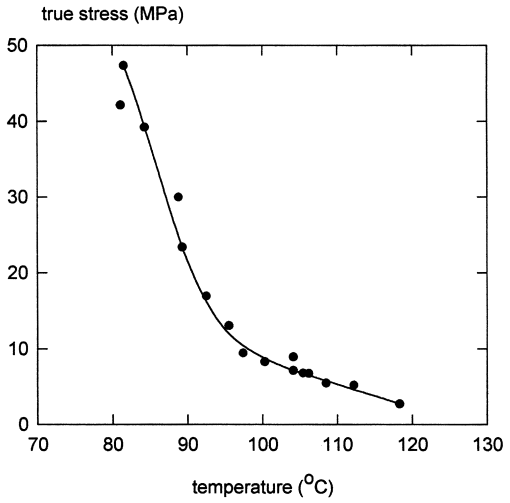

Fig. 9. Isometric plot of CW data generated for a nominal strain of 2.3: the plateau seen clearly in isometric plots for CW drawing at lower strains (see Fig. 6) is much less evident.

3.3. Determination of the contribution of entanglement slippage

The procedure described above, for isolating the rubber-like response at 80°C, was repeated with the results from CW and EB drawing experiments at higher temperatures. Here, it is to be expected that entanglement slippage contributes to the total stretch, and the resulting stress–strain relations may be considered "apparent" rubber-like responses, for the temperatures concerned and the prevailing nominal strain-rate (1/s). Sample results are shown in Fig. 12 for CW drawing. It can be seen that there was close agreement between curves obtained at temperatures near 80°C over the whole strain range, and at low strains over

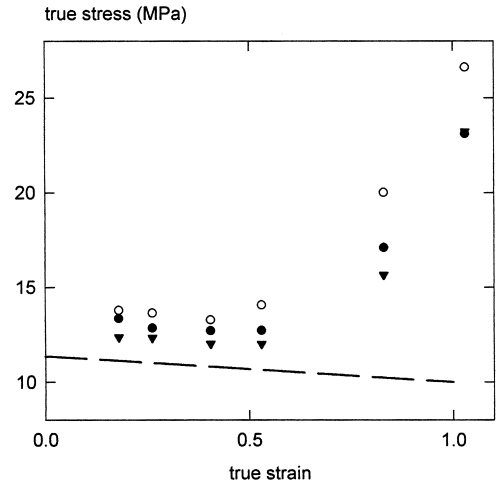

Fig. 10. Apparent "glassy" contribution to true stress plotted versus true strain, as deduced for CW drawing at 80°C, by subtracting the apparent rubber-like contribution from the total measured stress (see text). Dashed line shows the gradient expected from the Eyring model of flow. The deviation upwards at large strain is evidence for under-estimation of the rubber-like contribution.

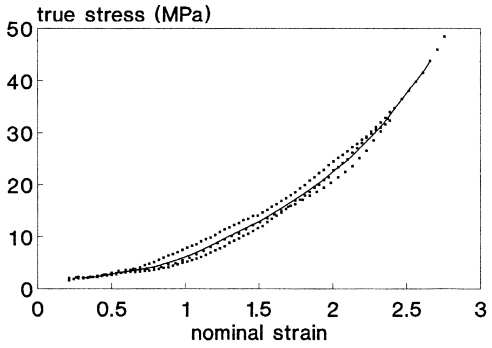

Fig. 11. Mean rubber-like stress–strain curve for CW stretching at 80°C (full line). Also shown (points) are the three data sets from which it was obtained: they were deduced from experimental data in nominally identical tests.

the whole temperature range up to 97°C shown here, confirming the hypothesis that entanglement slippage is negligible under these particular conditions. At higher temperatures and strains, however, there is a clear stress deficit.

In terms of the model, the stress deficit is caused by a contribution to strain from entanglement slippage, reducing the network stretch and hence the conformational stress, for a given total strain. In fact, data such as those shown in Fig. 12 enable the entanglement slippage stretch λ_1^s to be evaluated for any given apparent rubber-like stress, by use of Eq. (4) applied to the draw direction, given that the lowest temperature curve provides the network stretch λ_1^n.

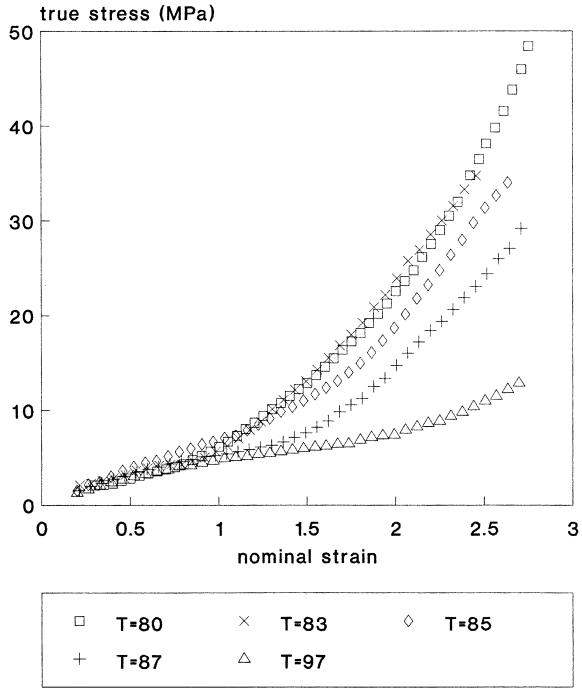

Fig. 12. Apparent rubber-like stress–strain curves for CW stretching, deduced from data from tests at various temperatures as shown. Close to 80°C there is agreement, but at higher temperatures there is increasing stress deficit, resulting from entanglement slippage.

In this manner, λ_1^s was determined from the present results for a variety of temperatures, for CW and EB drawing. Results are shown in Figs. 13 and 14. They reveal a remarkable anomaly. With increasing temperature the onset of entanglement slippage occurred sooner, as expected. However in every case except one (at the highest temperature in CW drawing) the slippage was arrested, at a value of λ_1^s which increased with temperature. At any particular temperature, the value of the maximum slippage stretch was always greater in the CW case than in the EB case. The explanation for this curious behaviour is to be found in structural change accompanying the drawing of PET, as discussed later.

The results plotted in Figs. 13 and 14 were examined to discover the criterion determining the arrest of entanglement slippage. It is clear from these graphs that the stresses required in the case of CW drawing were lower than those required in the case of EB drawing, and that the critical stresses decreased with increasing temperature. After fitting the rubber-like stress–strain curve to theory, the network stretches corresponding to the stresses shown in Figs. 13 and 14 were calculated, and hence three further possible criteria were considered: (1) the maximum principal network stretch λ_{max}^n, (2) the first invariant of the network stretch $I_1^n = \lambda_1^{n2} + \lambda_2^{n2} + \lambda_3^{n2}$, and (3) $\sqrt{I_1^n - 3}$. For each experiment shown in Figs. 13 and 14, the point was found where the slippage stretch had just ceased increasing to within experimental uncertainty, and the three criteria tested to find which gave the best correlation between the results of CW and EB tests, and with varying temperature. The best correlation, with a linear variation with temperature, was found using the arrest value of λ_{max}^n, which in the present experiments was the arrest value of the stretch λ_1^n. In the following, the critical value of this maximum network stretch is denoted by λ_{crit}. The resulting plot of λ_{crit} versus temperature, for CW and EB drawing, is shown in Fig. 15. It can be seen that even this correlation fails to bring the CW and EB data together to within experimental scatter: the correlation coefficient is 0.73. The equation of the regression line shown (with temperature T in °C) is

$$\lambda_{crit} = 5.6 - 0.037T. \quad (12)$$

4. Fitting of the extended constitutive model to data

4.1. Extension to the constitutive model

For the purpose of modelling film-drawing processes, it is desirable to express the mechanical response of the polymer in the form of a multiaxial constitutive model. The structure of such a model has been outlined in a previous section. With the role of entanglement slippage quantified as described above, it is possible to extend the model to incorporate this important feature, and hence to improve the prediction of strain-stiffening. The primary effect is to

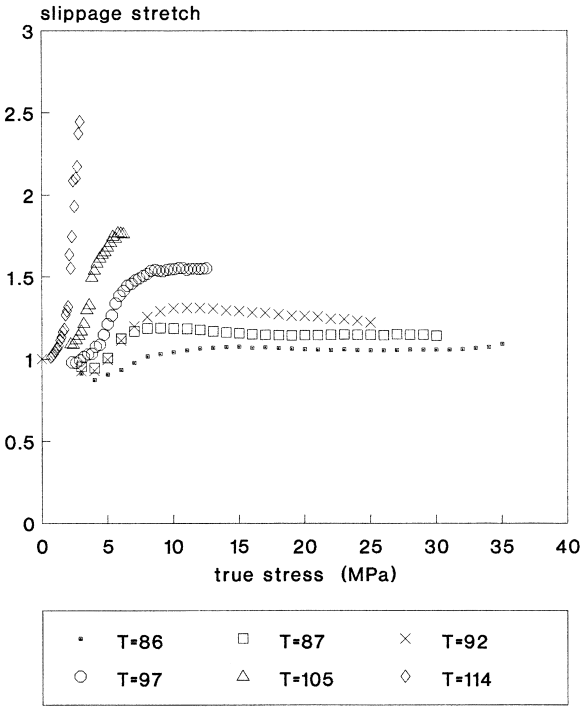

Fig. 13. Slippage stretch λ^{s} obtained from CW drawing tests at various temperatures (°C) shown. The slippage can be seen to arrest.

cause the conformational stresses σ_i^{c} to exhibit visco-elasticity, in a manner analogous to σ_i^{b} (see Eq. (7)); but in this case the elastic strains cannot be considered small.

The rate of true strain associated with entanglement

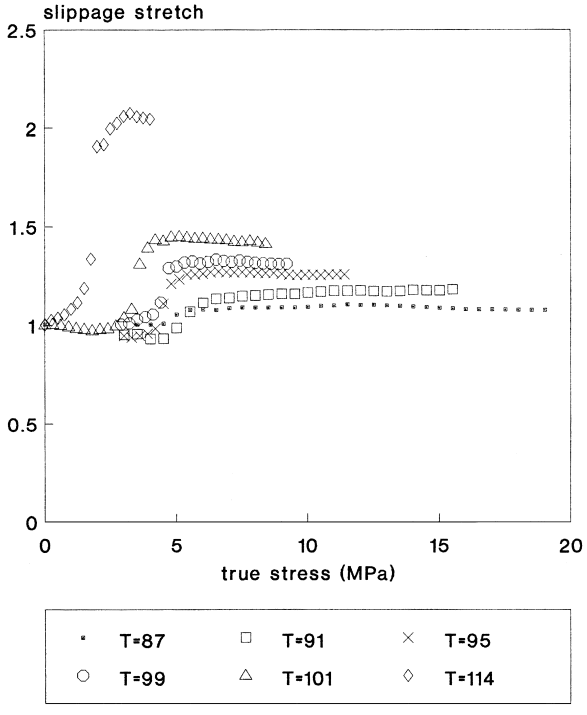

Fig. 14. As for Fig. 13, except for EB drawing.

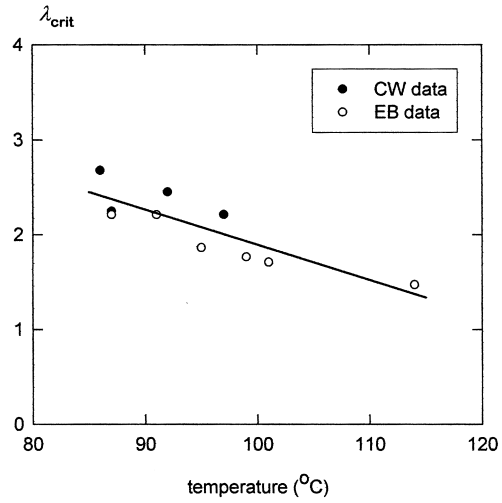

Fig. 15. The critical value of maximum principal network stretch λ_{max}^{n} for slippage arrest, as deduced from data from CW and EB drawing tests. Also shown (full line) is a linear regression through all the points shown.

slippage was expressed through a non-Newtonian flow-rule

$$\dot{\varepsilon}_i^{s} \equiv \frac{\mathrm{d}\ln\lambda_i^{s}}{\mathrm{d}t} = \frac{s_i^{c}}{\gamma} \qquad (i = 1\ldots3) \tag{13}$$

and its arrest was expressed in terms of the viscosity γ increasing asymptotically as the molecular orientation develops. Specifically, for consistency with the experimental observations reported above, γ was modelled as increasing without limit as λ_{crit} approached the critical stretch λ_{crit}, according to the simple two-parameter expression:

$$\gamma = \gamma_0\left(\frac{\lambda_{crit} - 1}{\lambda_{crit} - \lambda_{max}^{n}}\right), \tag{14}$$

where $\lambda_{max}^{n} < \lambda_{crit}$, and $\gamma^{-1} = 0$ otherwise.

The rate of true strain due to elastic network stretch was obtained by expansion in terms of rates of change of the stresses:

$$\dot{\varepsilon}_i^{n} \equiv \frac{\mathrm{d}\ln\lambda_i^{n}}{\mathrm{d}t} = \frac{1}{\lambda_i^{n}}\sum_{j=1}^{3}\frac{\partial\lambda_i^{n}}{\partial\sigma_j^{c}}\frac{\mathrm{d}\sigma_j^{c}}{\mathrm{d}t}. \tag{15}$$

Finally, to complete revision of the constitutive model described before [4], an expression for the full rate of logarithmic strain because of the conformational stress is assembled by combining Eqs. (13) and (15):

$$\dot{\varepsilon} = \frac{1}{\gamma}\left(\sigma_i^{c} - \frac{1}{3}\sum_{j=1}^{3}\sigma_j^{c}\right) + \frac{1}{\lambda_i^{n}}\sum_{j=1}^{3}C_{ij}^{c}\frac{\mathrm{d}\sigma_j^{c}}{\mathrm{d}t} \qquad (i = 1\ldots3), \tag{16}$$

where C_{ij}^{c} denotes an element of the tangent conformational compliance matrix $\mathbf{C}^{c}$ which in turn is obtained from the

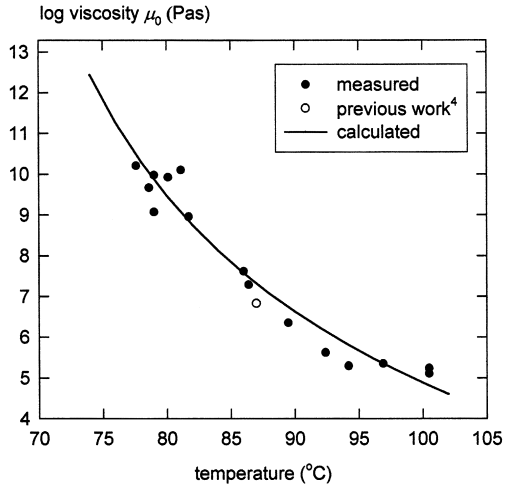

Fig. 16. Logarithm of viscosity μ_0 characterising relaxation of the bond-stretching stress, plotted versus temperature. The full line is a best fit to Eq. (18) with μ_0^*, C^v and T_∞ as disposable parameters. The open symbol gives the single value obtained previously by a different procedure [4].

tangent conformational stiffness matrix $\mathbf{G}^c$ as

$$\mathbf{C}^c = \mathbf{G}^{c-1} \qquad \text{where} \qquad G^c_{ij} = \frac{\partial \sigma^c_i}{\partial \lambda^n_j}. \tag{17}$$

Eq. (16) thus provides three additional equations to add to the set of six other simultaneous differential equations describing the material: the three equations corresponding to Eq. (16) but for the bond-stretching stress, and the three equilibrium equations (2). In the present work, solution of this set of equations was carried out numerically, employing central difference approximations of the first differentials in Eqs. (10), (16) and (17), and the direct integration method described elsewhere [4] for integration of Eq. (7) through the time-step. An alternative approach, where the equations of the same model are solved within the context of a commercially available finite element solver, has also been described recently [19].

4.2. Fitting of the constitutive model

The model in its new form (extended as above) has four component parts. We consider each in turn.

4.2.1. Linear elastic bond-stretching

Two elastic constants are required to describe the isotropic linear elasticity associated with bond-stretching. These were taken previously [4] to be the shear and bulk moduli: $G^b = 600$ MPa, and $K^b = 1800$ MPa respectively. The performance of the model is insensitive to the precise values of these under the conditions of interest (above the glass transition), and these values were used unchanged in the present work.

4.2.2. Viscoplastic flow

The required parameters are those that describe the variation of viscosity μ with stress and temperature (see Eq. (9)). The former is achieved through the two Eyring activation volumes that were determined in previous work [4]: the shear and pressure activation volumes $V_s = 7.23 \times 10^{-3}\,\mathrm{m^3\,mol^{-1}}$ and $V_p = 1.35 \times 10^{-3}\,\mathrm{m^3\,mol^{-1}}$, respectively. The temperature-dependence of the viscosity in the small-stress limit was assumed to take the Macedo and Litovitz hybrid form [18]:

$$\mu_0 = \mu_0 * \exp\left(\frac{C^v}{T_f - T_\infty} - \frac{C^v}{T_f * - T_\infty} + \frac{\Delta H_0}{RT} - \frac{\Delta H_0}{RT*}\right), \tag{18}$$

where μ_0* is the value for a reference temperature $T*$ and structural state (fictive temperature) T_f*. In the work reported here however, concerned only with temperatures above the glass transition, the amorphous polymer was assumed to be in metastable structural equilibrium, and the fictive temperature was assumed equal to the actual temperature ($T_f = T$).

The activation enthalpy ΔH_0 was again given the value 123 kJ/mol deduced previously from published viscoelasticity measurements on PET below the glass transition [4], while the remaining parameters C^v and T_∞ were determined from results of the present CW drawing experiments determined at 100°C or below. The first step was to determine the strain-induced bond-stretching stress $\Delta\sigma^b_1 (= \sigma^b_1 - \sigma^b_{m0})$ in the draw direction during viscoplastic flow, by subtracting the strain-induced conformational stress $\Delta\sigma^c_1$ from the total true stress σ_1. This was carried out after the rubber-like response had been fitted already to the Edwards–Vilgis theory, which therefore allowed $\Delta\sigma^c_1$ to be computed for given specimen stretch, in the absence of entanglement slippage. Thus $\Delta\sigma^b_1$ was found for stretches 1.2, 1.3 and 1.5, which were unaffected by entanglement slippage in the temperature range considered (see Fig. 12). Then the limiting viscosity μ_0 was found from these stresses by invoking the Eyring model of viscoplastic flow employed in the present constitutive model, applied to CW drawing, which gives (see Buckley et al. [4])

$$\mu_0 = \sqrt{6}\frac{\lambda_1}{\dot\lambda_1}\frac{RT}{V_s}\sinh\left(\frac{V_s\Delta\sigma^b_1}{2\sqrt{6}RT}\right)\exp\left(\frac{V_p\Delta\sigma^b_1}{2RT}\right). \tag{19}$$

The results were averaged at each temperature and then least squares fitted to Eq. (18) to yield best fit values of $\mu_0* = 19.7$ MPas (for $T* = 87$°C), $C^v = 439$K and $T_\infty = 56$°C. The data points are compared with the fitted line in Fig. 16. It can be seen that, especially at temperatures close to 80°C there was considerable scatter in experimental data (believed to reflect uncertainty in temperature measurements, combined with the strong temperature-dependence of viscosity in this region). Consequently the numerical values of the above parameters are subject to considerable uncertainty, but the fit to Eq. (18) is adequate for present purposes. Also included in Fig. 16 is an additional data point obtained for the same material but by a different route, in the

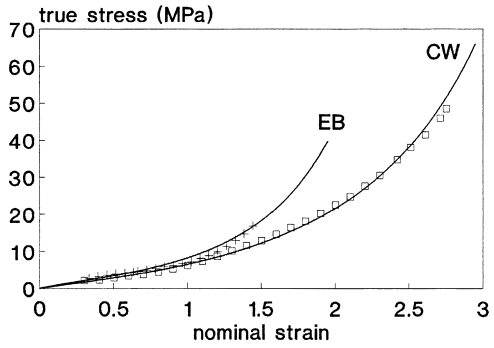

Fig. 17. True stress versus nominal strain for the PET rubber-like network, for CW and EB stretching at 80°C, as deduced from the present experimental data (points – see text), and as calculated from the Edwards–Vilgis theory (lines), after fitting to the CW data, with N_s, α and η as disposable parameters.

work reported earlier [4]: it is consistent to within experimental scatter.

4.2.3. Rubber-like elasticity

The mean rubber-like stress–strain curve for CW stretching, as deduced above, was compared with that predicted for CW stretching by the Edwards–Vilgis [30] theory of rubber elasticity, with the stress calculated using Eq. (10) and assuming constant volume deformation. Least-squares fitting of the theory to the data produced values for the three parameters: number of slip-links per unit volume $N_s = 2.75 \pm 0.15 \times 10^{26}\,\mathrm{m}^{-3}$, sliplink looseness factor $\eta = 0$, and inextensibility factor $\alpha = 0.164 \pm 0.001$. The quality of the fit may be seen in Fig. 17, where the data are compared with the fitted line.

To obtain an independent check on the validity of this fit, the same set of parameters was used with the E–V theory to predict the rubber-like stress–strain curve for EB stretching,

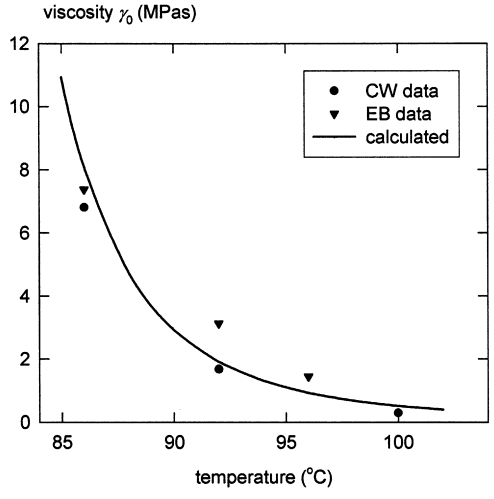

Fig. 18. Viscosity γ_0 characterising entanglement slippage versus temperature. Data points: values required for best-fits of simulations to experimental stress–strain curves; the line is a best fit to Eq. (20) with γ_0^* and C^s as disposable parameters.

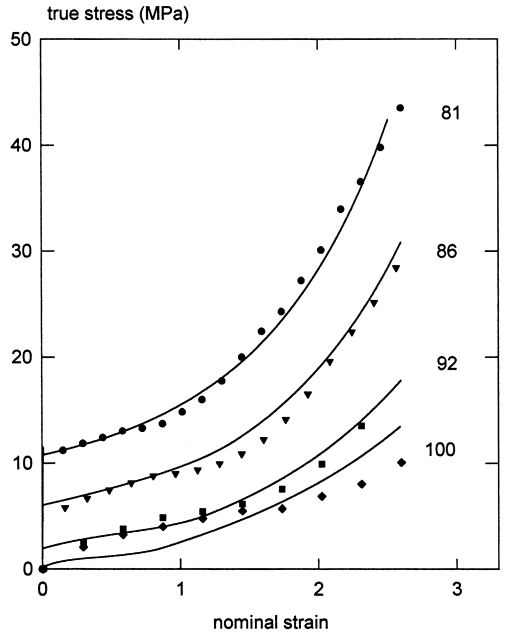

Fig. 19. Constant width (CW) drawing of PET at a constant extension-rate of 1/s and various temperatures (°C) shown: experimental data (points) and results of simulations with the constitutive model (lines).

and compared with data calculated from EB results at 80°C. The procedure used to obtain these was analogous to that described above for CW drawing. The calculated curve and experimental points are included in Fig. 17, where again there is close agreement. In particular, the E–V theory clearly succeeds in capturing the more rapid strain-stiffening seen in EB stretching, as compared to the CW case.

4.2.4. Viscous flow by entanglement slippage

In view of the proximity of the glass transition to the temperature range of interest, the temperature dependence of the initial melt viscosity γ_0 was expressed in terms of the Fulcher equation [31]

$$\gamma_0 = \gamma_0^* \exp\left(\frac{C^s}{T - T_\infty} - \frac{C^s}{T^* - T_\infty}\right) \tag{20}$$

with the same value of Vogel temperature T_∞ as found for Eq. (18). Values for the viscosity $\gamma_0(T)$ were found empirically, as those required to give best fits between measured stress–strain curves and those calculated in simulations of the same experiments using the full constitutive model, for a representative sub-set of the CW and EB data sets. Results are shown in Fig. 18, together with a curve showing the best fit of Eq. (20) through the points, which gave values $\gamma_0^* = 6.13$ MPa (at $T^* = 87$°C) and $C^s = 260$ K.

4.3. Comparison with experiment

The full constitutive model, incorporating new network parameters as obtained in the present work and the additional equations describing entanglement slippage, was

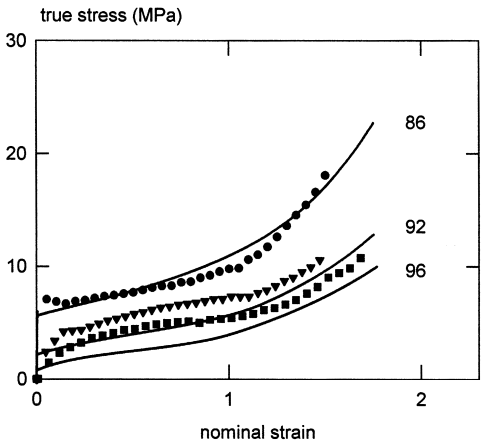

Fig. 20. As for Fig. 19, but for EB drawing.

tested against results of hot-drawing experiments under CW and EB conditions. Typical results are shown in Figs. 19 and 20 respectively. It is clear that the main objective of the present work has been achieved.

The revised model captures the observed deferral of strain-stiffening as temperature increases, and in terms of the model this is because of an increasing contribution to the total stretch arising from entanglement slippage. It is also clear that the model reproduces the overall shape of stress–strain curve better in the CW than the EB case. The major discrepancy is a systematic tendency for the model, when fitted to data as described above, to poorly estimate the stress at nominal strains less than 1 at the highest temperatures, especially in the case of EB drawing. This is a symptom of the major known weakness of the model in the form described here. As it describes viscoplastic flow as a single flow process, the predicted yield event is sharper than observed experimentally, as discussed previously [4], and cannot be modelled accurately without the introduction of a relaxation spectrum. Nevertheless, the addition to the model of a temperature-dependent viscosity $\gamma_0(T)$ and an arrest criterion λ_{crit} can be seen to have made possible a reasonable representation of the temperature-dependence of strain-stiffening at large strains.

5. Discussion

5.1. Parameters of the PET network

The apparent entanglement density N_s deduced from fitting data to the E–V theory provides a value of the density of chains N making up the network: they are related through a factor g, with $N = gN_s$. Strict interpretation of entanglements as tetrafunctional junction points would imply $g = 2$. In practice, however, by analogy with the long-established case of cross-linked elastomers [32] a better assumption appears to be $g = 1$, and even this is probably an over-estimate. The density of chains determined here in this way ($N = 2.75 \times 10^{26}\ m^{-3}$) is significantly higher than the value $1.67 \times 10^{26}\ m^{-3}$ obtained in the earlier study using the same PET film [4]. The difference is because of inadequate removal of the effects of entanglement slippage in the previous work. In the recent work by Mathews et al. [5], in which stress–strain data for PET was fitted to the E–V theory (in an earlier form which took $\alpha = 0$), a range of values of N was obtained depending on strain-rate: 2.5×10^{26}–$4.8 \times 10^{26}\ m^{-3}$, for octahedral shear rates $\dot{\gamma} = 5 \times 10^{-4}$–$5 \times 10^{-2}\ s^{-1}$. Within this range, the lower end is likely to be most reliable. Mathews et al. fitted the theory to total stress without subtraction of any contribution from bond-stretching, on the basis that earlier work [11] had demonstrated the validity of this approach at the temperature considered (85°C). In fact the evidence from earlier work was from the lower end of the strain-rate range ($\dot{\gamma} \approx 3 \times 10^{-3}$ s), raising the possibility that the apparent variation in N arose from residual bond-stretching stress at higher strain-rates. All these values, however, lie within the range of reported values of N from a variety of sources as discussed earlier [4].

When allowance is made for the effects of 'dangling ends' by means of the Flory correction factor [4], the value of N obtained in the present work corresponds to a molecular weight between entanglements of $M_e = 2240$, indicating that each network chain contains 11.7 monomers, corresponding to a number $n' = 70$ main-chain bonds (taking the whole phenyl group as one virtual bond). The factor α obtained from fitting the present data to the E–V theory provides the number of freely orienting segments between entanglements $n = 1/\alpha^2 = 37.2$. Thus, the network parameters obtained in the present work, in which there can be greater confidence than hitherto that there is no distortion from unrelaxed bond-stretching or the onset of entanglement slippage, have not resolved the anomaly identified in the previous article concerning flexibility of the PET chain. The derived value for the ratio $n'/n = 1.9$ is even further from those obtained by other routes; for example ca.9 as obtained from the characteristic ratio C_∞ for PET. The origins of this discrepancy with other measures of chain flexibility are not known for certain. However, the most likely causes are partly theoretical and partly experimental: (a) deficiencies remaining in current theories of rubber elasticity, leading to N as determined above being an over-estimate, and (b) residual entanglement slippage affecting the apparent rubber–elastic network stress–strain data, even after the precautions described above, leading to the calculated value of α being an under-estimate, and hence the n value deduced from it being too high.

For the third parameter η, there was agreement with the value zero obtained previously [4], indicating that entanglements in PET have little freedom to slide along the chain, perhaps because of the bulk of the phenyl groups. It is noteworthy, however, that the work of Mathews et al., concentrating on the initial part of stress–strain curves with different degrees of biaxiality, gave best-fit values of

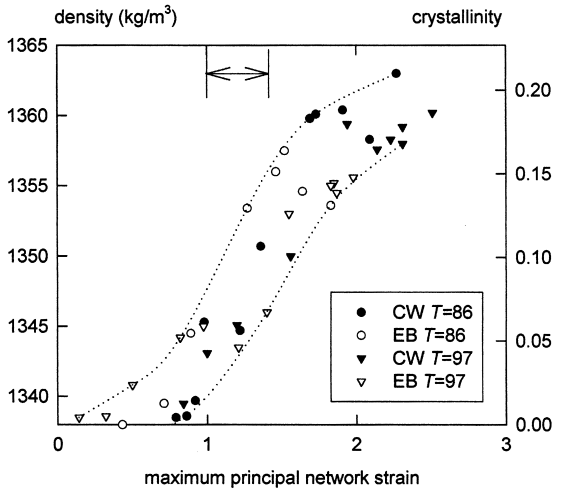

Fig. 21. The density data for CW and EB drawn specimens of Figs. 3 and 4, plotted together versus maximum principal network strain $\lambda^n_{max} - 1$. The data for different strain states and different temperatures all lie within the sigmoidal band shown. Also shown (double arrow) is the range of critical network strain $\lambda_{crit} - 1$ for entanglement slippage arrest, for the temperature range 86°C–97°C. It is clear that rapid stress-induced densification coincides with the arrest of entanglement slippage.

ca. 0.09. This may indicate that the E–V theory cannot provide a close fit to data over a wide range of strain, with a single set of parameters.

5.2. Entanglement slippage and its arrest

The reducing elastic effectiveness of entanglements, seen in the well-known deferral of strain-stiffening with rise in temperature, has been interpreted here in terms of the viscous flow associated with entanglement slippage. However, such an approach diverges from that of some authors and deserves a word of comment. The point has been made several times over the years that similar behaviour can be described in terms of a rubber– elastic network in which N reduces with increase in temperature or decreasing strain-rate. No precise mechanism is proposed, but it is speculated to be because of some form of thermally activated decay in the density of these physical network junction points. The case of PET was discussed in these terms by Mathews et al. [5] invoking an Eyring-type rate dependence for N, previously applied successfully to hot-drawing of poly(vinyl chloride) [33,34].

Which is the more accurate description cannot be decided on the basis of monotonic-loading experiments alone: significant differences in predicted behaviour would appear only under more complex loading histories. The approach adopted in the present work was chosen because of its practical utility in constitutive modelling: (a) it is consistent with the classical theory of linear viscoelasticity at vanishingly small stresses (deviatoric response in the rubbery region reduces to that of a single Maxwell element), and (b) it does not present difficulties in cases where strain-rate and temperature vary arbitrarily with time (as may be the case in modelling an actual manufacturing process), whereas the alternative approach may require unphysical (perhaps abrupt) changes in N to be assumed in such cases.

The most remarkable feature to emerge from the present work was the evidence for arrest of entanglement slippage. In terms of the model: as the flow corresponding to entanglement slippage is described by a viscosity γ, this arrest implies $\gamma \rightarrow \infty$. The phenomenon is most likely to be associated with the stress-induced crystallisation that accompanies drawing in PET in the temperature range considered. The increases in density and the appearance of WAXS diffraction spots observed in this work on specimens quenched after drawing to sufficiently high draw ratios, together confirm the onset of crystallinity in the present tests.

Evidence for a quantitative link between the arrest of entanglement slippage and structural change can be seen by comparing the strain levels at which they occur. Fig. 15 shows the arrest to occur at a maximum network stretch $\lambda^n_{max} = \lambda_{crit} \approx 2$, decreasing gently with rise in temperature. There have been numerous previous reports on the onset of stress-induced crystallinity in PET, when hot-stretched to a draw-ratio in this region or higher. Moreover, measurements have shown: (a) at fixed temperature, the degree of crystallization correlates with the degree of molecular orientation in the amorphous fraction (expected to correlate with λ^n_{max}) [35,36], and (b) the orientation required to achieve a given degree of crystallinity decreases with increase in temperature [35]. Both (a) and (b) are consistent with the present proposal that the viscosity γ is increased by crystallinity and that this may be expressed via Eqs. (12) and (14). The fact that crystallisation is found to be deferred to higher total stretch λ with decreasing strain-rate or increasing temperature [24–26], is easily explained in terms of the present model, as resulting from an increasing contribution of slippage stretch λ^s leading to reduced λ^n for given λ.

To test this interpretation using data from the present study, density measurements obtained from tests at different temperatures, as shown in Figs. 3 and 4, were re-plotted on a common basis with the maximum principal network strain $\lambda^n_{max} - 1$ as abscissa, using Eq. (4) to correct the measured total stretch for the slippage stretch, already determined. The composite plot is given in Fig. 21, where data for CW and EB drawing and the two different temperatures can be seen to merge together to within the scatter, and to lie within the single S-shaped envelope drawn. The inflection of the "S" extrapolates back to an estimated intercept at $\lambda^n_{max} \approx 2$. The reader will recall that discrete X-ray diffraction peaks were first discernible in the WAXS patterns at a stretch of 2.3 (see Table 1).

The coincidence of these features, observed in different measurements, strongly suggests a causal link. The clear inference is that crystallisation is triggered by increasing molecular orientation, and is definitely visible when $\lambda^n_{max} \approx 2$. This causes a slow-down and arrest of entanglement slippage, presumably because of the extra topological

constraint imposed at the molecular level by the developing crystallinity, as proposed by Buckley and Salem [37]. The mechanism may be considered to be mechanically analogous to the rapid increase in viscosity of a liquid polymer during a chemical crosslinking reaction. A point of particular interest is the rapidity of the arrest of entanglement slippage as seen in Figs. 14 and 15. According to the above picture of events, the likely explanation is the autocatalytic nature of the process. The presence of a trace of crystallinity causes a reduction in the rate of entanglement slippage and hence an increase in the rate of network stretch, i.e. of amorphous orientation, leading to faster crystallisation, and even slower slippage and faster network stretch. Slippage is thus arrested completely, on the time-scale of the experiment.

This explanation neatly ties together several disparate pieces of experimental evidence, and appears to form a coherent physical basis for the constitutive model. However it is challenged by recent, simultaneous real-time wide-angle X-ray scattering patterns and video images of PET film during rapid hot-drawing (nominal strain-rate ca. $10\ s^{-1}$), obtained with synchrotron X-ray sources [38,39]. These experiments showed that a critical degree of molecular orientation is required for crystallization to occur (as manifest by X-ray diffraction). Moreover, at such rates stress-induced crystallization apparently did not occur until drawing terminated, *whatever the draw ratio reached*.

The evidence so far is not conclusive. The crystal (*hk*0) diffraction peaks cannot be resolved reliably in these experiments for degrees of crystallinity below ca. 10%. Nevertheless, it implies that crystallinity found in drawn specimens originated after drawing, and therefore cannot be used to explain mechanical effects during drawing. Further, crystallinity cannot be responsible for mechanical effects observed at strains below those required to induce crystallization. By contrast the present data reveal (Figs. 13 and 14), and the model describes (Eq. (14)), effects of structure development beginning at lower strains. We are forced to conclude that the arrest of slippage is caused by molecular association beginning prior to crystallization; without the long-range order needed to give discrete X-ray diffraction, but nevertheless providing topological constraint on molecules and inhibiting slippage of entanglements. One might speculate that groups of mutually aligned trans segments associate by π-bonding between phenyl groups, but without lying in crystallographic register. Only if the degree of orientation exceeds a critical value (corresponding to a maximum principal network stretch of ca. 2) is this association rendered permanent by the nucleation of crystals.

6. Conclusions

The purpose-built biaxial testing machine FBFT has made possible a new study of drawing of PET films, under conditions of strain-state, strain-rate and temperature relevant to biaxial orientation processes used in manufacture of PET products. This provided the biaxial stress–strain data needed to construct a multiaxial constitutive model for the hot-drawing of PET. In particular, it allowed the glass–rubber constitutive model proposed earlier [4] to be developed further, to encompass the additional features of entanglement slippage and crystallisation, and hence to describe better than hitherto the strain-stiffening of PET across the time-temperature range of practical interest. The device of representing entanglement slippage as an additional stretch superposed on the stretch of an elastic network has proved especially useful. It was this that allowed the effect of entanglement slip on strain-stiffening to be quantified objectively, and in the present case of PET it led to a remarkable observation. The slippage arrested spontaneously at a critical degree of molecular orientation, as expressed through a critical degree of stretch of the entanglement network. In three dimensions this occurred at a maximum principal network stretch λ^{n}_{max} of approximately 2, decreasing with increase in temperature. Within the constitutive model, it was possible to capture the effect adequately by introducing a simple one-parameter expression for the variation of viscosity with λ^{n}_{max}.

It is clear from the many items of structural evidence, including some from the present work obtained on specimens from the mechanical tests, that this arrest of entanglement slippage is connected with the appearance of crystallinity in the drawn specimens. However the precise mechanism is not yet known. The association of individual chains to form crystals is expected to lead to increased topological constraint, and hence increased viscosity [37]. However, the recent real-time X-ray evidence that diffraction appears only after drawing ceases, at high draw-rates, suggests that structural entities causing the viscosity rise do not have the long-range order of crystals, but nevertheless can lead to eventual crystallization.

With respect to the numerical simulation of biaxial hot-drawing in PET, the three-dimensional constitutive model described here has been reasonably successful. With 14 parameters it describes the rate and temperature-dependence of finite strain, biaxial drawing of initially amorphous PET, from the glass transition region through the rubbery plateau and into the terminal region. Its chief known deficiency is its simplification of viscoelasticity as two single relaxation-time processes, but it is straightforward to introduce relaxation spectra, in any application where the improvement in accuracy merits the additional computing cost. An illustration is provided by the recent work of Dooling et al. [16], where a small strain version of the model was used to describe in detail the nonlinear viscoelastic creep of glassy PMMA in the region of T_g.

Having been tested against monotonic straining experiments such as those described here, the model now needs to be tested against a wider range of strain sequences, including stress relaxation following biaxial drawing, and

sequential biaxial drawing, of importance in several industrial orientation processes. Some progress has been reported already, for both stress relaxation [40] and sequential biaxial drawing [41]. Early indications are that the onset of stress-induced crystallinity causes certain specific additional features in the constitutive response that need representation in the constitutive model. Nevertheless, the general structure of the model remains applicable.

Acknowledgements

The authors acknowledge the support of the UK Science and Engineering Research Council and ICI plc, through the award of a CASE Research Studentship to AMA. They are also indebted to Mr B. Lewis and Dr D. Blundell of ICI, for providing the density measurements and wide-angle X-ray diffraction patterns respectively.

References

[1] Chandran P, Jabarin S. Adv Polym Techn 1993;12:119.
[2] Chandran P, Jabarin S. Adv Polym Techn 1993;12:133.
[3] Chandran P, Jabarin S. Adv Polym Techn 1993;12:153.
[4] Buckley CP, Jones DC, Jones DP. Polymer 1996;37:2403.
[5] Mathews RG, Duckett RA, Ward IM. Polymer 1997;38:4795.
[6] Zaroulis JS, Boyce MC. Polymer 1997;38:1303.
[7] Pinnock PR, Ward IM. Trans Faraday Soc 1966;62:1308.
[8] Rietsch , Duckett A. Ward. I.M. Polymer 1979;20:1133.
[9] Long SD, Ward IM. J Appl Polym Sci 1991;42:1911.
[10] Long SD, Ward IM. J Appl Polym Sci 1991;42:1921.
[11] Gordon DH, Duckett RA, Ward IM. Polymer 1994;35:2554.
[12] Ward IM. Polym Eng Sci 1984;24:724.
[13] Haward RN, Thackray G. Proc Roy Soc A 1968;302:453.
[14] Boyce MC, Arruda EM. Polym. Eng. Sci. 1990;30:1288.
[15] Hasan OA, Boyce MC. Polym Eng Sci 1995;35:331.
[16] Dooling PJ, Buckley CP. Hinduja. S Polym Eng Sci 1998;38:892.
[17] Bergstrom JS, Boyce MC. J Mech Phys Solids 1998;46:931.
[18] Buckley CP, Jones DC. Polymer 1995;36:3301.
[19] Gerlach C, Buckley P, Jones DP. Trans I Chem E 1998;76 Part A:38.
[20] Adams AM, D.Phil thesis. University of Oxford, 1995.
[21] Buckley CP, Sikorski ME. J Text Inst 1991;82:25.
[22] Adams AM, Buckley CP, Jones DP. Polymer 1998;39:5761.
[23] Alexander LE. X-ray diffraction methods in Polymer Science. New York: Wiley, 1969.
[24] Salem DR. Polymer 1992;33:3182.
[25] Salem DR. Polymer 1992;33:3189.
[26] Salem DR. Polymer 1994;35:771.
[27] Adams AM, Buckley CP, Jones DP. Polymer Processing Society European Regional Meeting, Strasbourg, 1994.
[28] Lee EH. ASME. J Appl Mech 1969;36:1.
[29] Halsey G, White HJ, Eyring H. Text Res J 1945;15:295.
[30] Edwards SF, Vilgis T. Polymer 1986;27:483.
[31] Ferry JD. Viscoelastic properties of polymers. 3. New York: Wiley, 1980.
[32] Treloar LRG. The physics of rubber elasticity. 3. Oxford: Clarendon Press, 1975.
[33] Sweeney J, Ward IM. Trans I Chem E 1993;71:232.
[34] Sweeney J, Ward IM. Polymer 1995;36:299.
[35] Le Bourvellec G, Monnerie L, Jarry JP. Polymer 1987;28:1712.
[36] Clauss B, Salem DR. Polymer 1992;33:3193.
[37] Buckley CP, Salem DR. Polymer 1987;28:69.
[38] Blundell DJ, MacKerron DH, Fuller W, Mahendrasingam A, Martin C, Oldman RJ, Rule RJ. Riekel. C. Polymer 1996;37:3303.
[39] Mahendrasingam A, Martin C, Fuller W, Blundell DJ, Oldman RJ, Harvie JL, MacKerron DH, Riekel C, Engstrom, P. Polymer, in press.
[40] Adams AM, Buckley CP, Jones DP. Proceedings of the symposium on mechanics of plastics and plastics composites. ASME International Mechanical Engineering Congress and Exposition 1995;MD68:365–374.
[41] Gerlach C, Buckley CP, Dooling PJ, Jones DP, Proceedings of the 14th Annual Meeting of the Polymer Processing Society, Yokohama, 1998.